



## Microseisms from Superstorm Sandy



Oner Sufri<sup>a</sup>, Keith D. Koper<sup>a,\*</sup>, Relu Burlacu<sup>a</sup>, Benjamin de Foy<sup>b</sup>

<sup>a</sup> Department of Geology and Geophysics, University of Utah, Salt Lake City, UT 84112, United States

<sup>b</sup> Department of Earth and Atmospheric Science, Saint Louis University, St. Louis, MO 63108, United States

### ARTICLE INFO

#### Article history:

Accepted 7 October 2013

Available online 1 November 2013

Editor: P. Shearer

#### Keywords:

USArray  
microseisms  
polarization analysis

### ABSTRACT

We analyzed and visualized the microseisms generated by Superstorm Sandy as recorded by the Earthscope Transportable Array (TA) during late October through early November of 2012. We applied continuous, frequency-dependent polarization analysis to the data and were able to track the course of Sandy as it approached the Florida coastline and, later, the northeastern coast of the U.S. The energy level of Sandy was roughly comparable to the background microseism level generated by wave–wave interactions in the North Atlantic and North Pacific oceans. The maximum microseismic power and degree of polarization were observed across the TA when Sandy sharply changed its direction to the west–northwest (specifically, towards Long Island, New York) on October 29. The westward turn also briefly changed the dominant microseism period from 5 s to 8 s. We identified three other microseismic source regions during the 18 day observation period. In particular, peak-splitting in the double frequency band and the orientation of the 5 s and 8 s polarization vectors revealed two contemporaneous microseism sources, one in the North Atlantic and one in the Northeast Pacific, for the dates of November 3–4. Predictions of microseismic excitation based on ocean wave models showed consistency with the observed microseismic energy generated by Sandy and other storms.

© 2013 Elsevier B.V. All rights reserved.

### 1. Introduction

It is well known that hurricanes, typhoons, and other oceanic storms create microseisms with periods of ~1–20 s at land-based seismometers, even those located thousands of kilometers inland from coastlines. Owing to relatively recent deployments of mid- and large-aperture arrays of broadband seismometers, it is now possible to study the complete wavefield of these signals, leading to improved location of microseismic sources and a deeper understanding of the underlying source mechanism.

Recent examples of these types of studies include detections of body and surface waves in southern California from 2005 Hurricane Katrina in the Gulf of Mexico (Gerstoft et al., 2006); location of microseismic sources in the Mediterranean Sea and northern Atlantic Ocean in the boreal winter of 2005–2006 using several variable-aperture arrays in western Europe (Chevrot et al., 2007); detection and location of teleseismic P waves throughout the world's oceans recorded by arrays in Yellowstone, Kyrgyzstan, and Turkey in 2000–2001 (Landes et al., 2010); tracking of western Pacific typhoons in 2006 using data recorded across Japan and Taiwan (Chi et al., 2010); analysis of Hurricane Irene and other storms in 2011–2012 using Transportable Array (TA) stations in the cen-

tral U.S. (Traer et al., 2012); observations from a temporary array deployed in 2002 in New Zealand of differing source regions for Love and Rayleigh waves created by Southern Ocean storms (Behr et al., 2013); and validation of microseismic P waves recorded at the Southern California Seismic Network (Obrebski et al., 2013).

While the basic theory of excitation for microseismic Rayleigh waves has been known for decades (e.g., Longuet-Higgins, 1950; Hasselmann, 1963) general uncertainties still exist in terms of source locations and mechanisms, such as the relative importance of coastal reflections vs. deep water storm interactions in generating double-frequency microseisms, and the details of how strong transverse energy (Love waves) can be generated by the fluid ocean interacting with the solid Earth. The recent development of sophisticated, realistic ocean wave models and theoretical advances in fluid dynamics now allow for quantitative simulation of microseisms (Kedar et al., 2008; Arduin et al., 2011; Arduin and Herbets, 2013), and therefore a current motivation for studying microseisms is to better understand fundamental interactions between the coupled atmosphere–ocean–solid Earth system. This topic was listed fourth in a recent top-ten list of “Seismological Grand Challenges” (Lay, 2009), and is one that will likely become increasingly important in the future as the geophysical effects of climate change are identified and studied.

A specific theme in microseismic research that has emerged is mining historical seismic data to develop a baseline of severe storm occurrence in pre-satellite days when hurricanes, typhoons, and so on were likely undercounted or poorly documented

\* Corresponding author. Tel.: +1 801 585 3669; fax: +1 801 585 5585.

E-mail addresses: osufri@seis.utah.edu (O. Sufri), koper@seis.utah.edu (K.D. Koper), burlacu@seis.utah.edu (R. Burlacu).

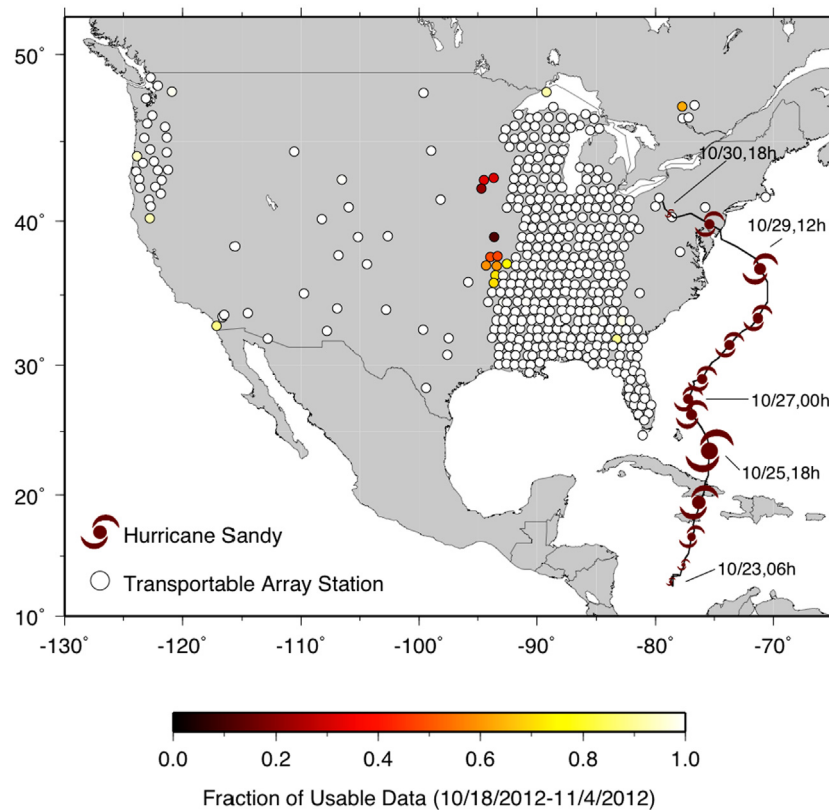


**Fig. 1.** Map of TA station geometry during the time Superstorm Sandy was active. Circles indicate seismometer locations, with color indicative of data completeness. The track of Sandy is shown using hurricane symbols equally spaced in time from October 22, 2012 through November 1, 2012, with symbol size proportional to wind speed.

(Landsea, 2007). This allows for quantitative comparisons with more recent seismic observations of storm activity to determine whether storm frequency and intensity have increased over the last 50–60 yr as global temperatures have risen (Grevemeyer et al., 2000; Ebeling and Stein, 2011); more generally it complements seismic monitoring of changes in the ocean wave climate that capitalize on the broad geographical sensitivity of microseisms (Aster et al., 2008; Koper et al., 2009; Stutzmann et al., 2009; Aster et al., 2010).

In this study, we report on microseisms created by Superstorm Sandy that were recorded by stations of the TA deployed mostly in central and eastern U.S. during the period of October 22–31, 2012. Although at its peak Sandy was classified only as Category 3 (out of 5) on the Saffir–Simpson hurricane wind scale (<http://www.nhc.noaa.gov/aboutsshws.php>), it was the largest Atlantic hurricane on record as measured by spatial extent, and caused enormous damage along the east coast of the United States. We perform continuous, frequency-dependent polarization analysis of the TA data to determine how microseismic waves created by Sandy varied in time, space, power, coherence, and polarization, and compare these to meteorological observations of Sandy and predictions of microseismic power based on ocean wave models. We also compare the seismic observations of Sandy to the background microseismic field generated over a slightly longer time period (October 18–November 4, 2012).

## 2. Data and methodology

We downloaded all available broadband seismic data (channel codes of BHZ, BHN, and BHE) with the TA network code from the IRIS Data Management Center (DMC, [www.iris.edu](http://www.iris.edu)) for the days of October 18, 2012 through November 4, 2012 (GMT), corresponding to 432 potential hours of data for each station. For a given

hour of station data to be viable, we required there to be no gaps on all three components. Overall the data return was excellent, with 403 of the 428 stations meeting this requirement for all 432 hours (Fig. 1). We selected an hour as the fundamental unit of time in which to process the data because initial work showed that over this time period microseisms are relatively stationary and tend to overwhelm signals from transient events, such as small-to-moderate sized regional earthquakes.

The technique we used to process the data is described in detail in Koper and Hawley (2010). It is based on eigen-decomposition of  $3 \times 3$  spectral covariance matrices at individual stations, and follows the work of Sampson (1983) as described by Park et al. (1987). Cross-spectra are calculated only between different components of a single station and not between like components of different stations, so it is fundamentally a polarization analysis and not a conventional f–k or beamforming analysis. Advantages of the polarization approach over beamforming include (1) seismic energy does not have to be coherent between stations, (2) seismic energy does not have to propagate as a plane wave, and (3) true amplitudes are recovered because there is no beam loss. The main disadvantage is that polarization analysis tends to give more scattered estimates of backazimuth than does beamforming, especially when the signal-to-noise ratio is small (Harris, 1990; Suteau-Henson, 1990; Schulte-Pelkum et al., 2004).

Our approach is similar to the analyses of Tanimoto et al. (2006) and Schimmel et al. (2011) in that it operates in the frequency domain and polarization information, such as the degree of elliptical particle motion, is determined from phase differences among the components of a complex vector. In this respect it is different from techniques that extract polarization information from the relationship among the three eigenvalues of a purely real  $3 \times 3$  covariance matrix calculated in the time domain (e.g., Jurkevics, 1988; Earle, 1999; Schulte-Pelkum et al., 2004).

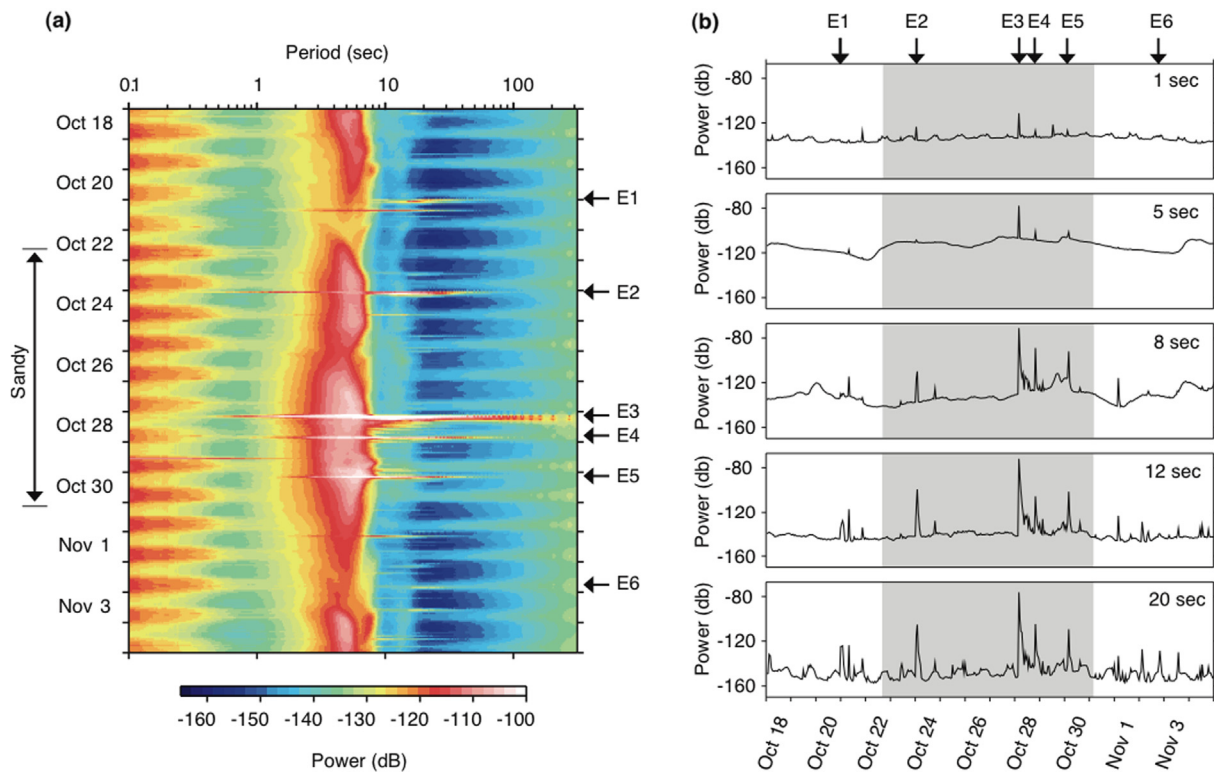


**Fig. 2.** (left) Array-averaged spectrogram of the dominant eigenvalue of the spectral covariance matrix. Earthquakes appear as horizontal lines and those with magnitudes larger than  $M_w$  6.0 are highlighted with arrows: E1 –  $M_w$  6.2 event in Vanuatu, E2 –  $M_w$  6.5 event in Costa Rica, E3 –  $M_w$  7.8 event in Haida Gwaii, E4 –  $M_w$  6.3 event in Haida Gwaii, E5 – and  $M_w$  6.2 event in Haida Gwaii, and E6 – an  $M_w$  6.1 event in the Philippines. (right) Array-averaged values of power for the dominant eigenvalue of the spectral covariance matrix across a range of periods in the microseism band of  $\sim 1$ –20 s. Grey shading is used for the time when Sandy was active.

Each hour-long segment of data is detrended and restored to ground acceleration by spectral division of the instrument response using a trapezoidal frequency-domain taper defined with frequency limits of 0.001–0.002 Hz and 10–20 Hz. Next, it is divided into 10 subwindows of length 819.2 s (32768 points) that overlap one another by 62%. Each subwindow is detrended, tapered with a 10% Hanning window, and processed with a fast Fourier transform (FFT). The spectral covariance matrix for the subwindow is computed by multiplying the FFT of each component by the complex conjugate of each component, and the overall spectral covariance matrix for the hour is computed by linear averaging of the subwindow matrices. A  $\log_{10}$ -based smoothing scheme is used to reduce the number of independent frequency bins from 32768 to 301, with the lowest bin centered at 0.00123 Hz and the highest at 19.9 Hz. The diagonal elements of the spectral matrix are estimates of the power spectral density (PSD) for each component and are output and saved for each hour-long segment of data at each station.

We next perform eigen-decomposition of each matrix and save the values of the dominant eigenvalue ( $\lambda$ ) and eigenvector, as well as the degree of polarization,  $\beta^2$ , which varies from 0, when the three eigenvalues are equal, to 1 when only a single non-zero eigenvalue exists (Samson, 1983). Polarization information is extracted from the complex dominant eigenvector (i.e., the eigenvector associated with the largest eigenvalue) as discussed by Park et al. (1987) to yield the following four angular quantities:  $\Theta_H$ , the horizontal azimuth of the major axis, which points in the direction of the source for P-waves, and varies from  $-180^\circ$  to  $180^\circ$ ;  $\Theta_V$ , the angle made with the vertical by the major axis of the ellipse, which corresponds to the angle of incidence for P waves, and varies from  $0^\circ$  to  $90^\circ$ ;  $\varphi_{HH}$ , the phase difference between the horizontal components, which varies from  $0^\circ$  to  $180^\circ$  and represents the degree of ellipticity in the horizontal plane; and  $\varphi_{VH}$ ,

the phase difference between the vertical and principal horizontal components, which varies from  $-90^\circ$  to  $90^\circ$  and represents the degree of ellipticity in that plane, for instance being  $-90^\circ$  for a pure retrograde Rayleigh wave.

### 3. Results

#### 3.1. Time evolution of array-averaged microseismic power

There is strong variability in microseism power as a function of frequency. The double-frequency, or secondary, peak is usually the largest in the microseismic band, and although it is centered at periods of 4–5 s on average (Peterson, 1993), it can vary significantly based on the distance from the source region to the station, the near-source bathymetry, and the details of the wave-wave interactions at the ocean's surface. Likewise, the single-frequency, or primary, peak that is centered at periods near 15 s on average (Peterson, 1993) can drift a few seconds in either direction. Furthermore, oceanic storms can excite seismic energy at periods both smaller (e.g., Koper et al., 2009) and larger (e.g., Rhie and Romanowicz, 2004) than the classic microseismic range.

We explore this issue for Sandy by calculating the array-averaged power as a function of time for each of the 301 frequency bins. This is presented as a spectrogram in Fig. 2(a). Power was calculated from the largest eigenvalue of the spectral matrix. This quantity is indicative of the dominant microseismic mode of propagation, no matter how the wavefield is polarized or from what direction it arrives at a station. It is a convenient way to reduce the number of dependent variables from 3 to 1 for visualization purposes. Fig. 2(b) shows slices of the spectrogram throughout the microseismic band, at periods of 1 s, 5 s, 8 s, 12 s, and 20 s.

As expected, the 5 s period has the largest power and is least affected by transient energy from earthquakes, which include the

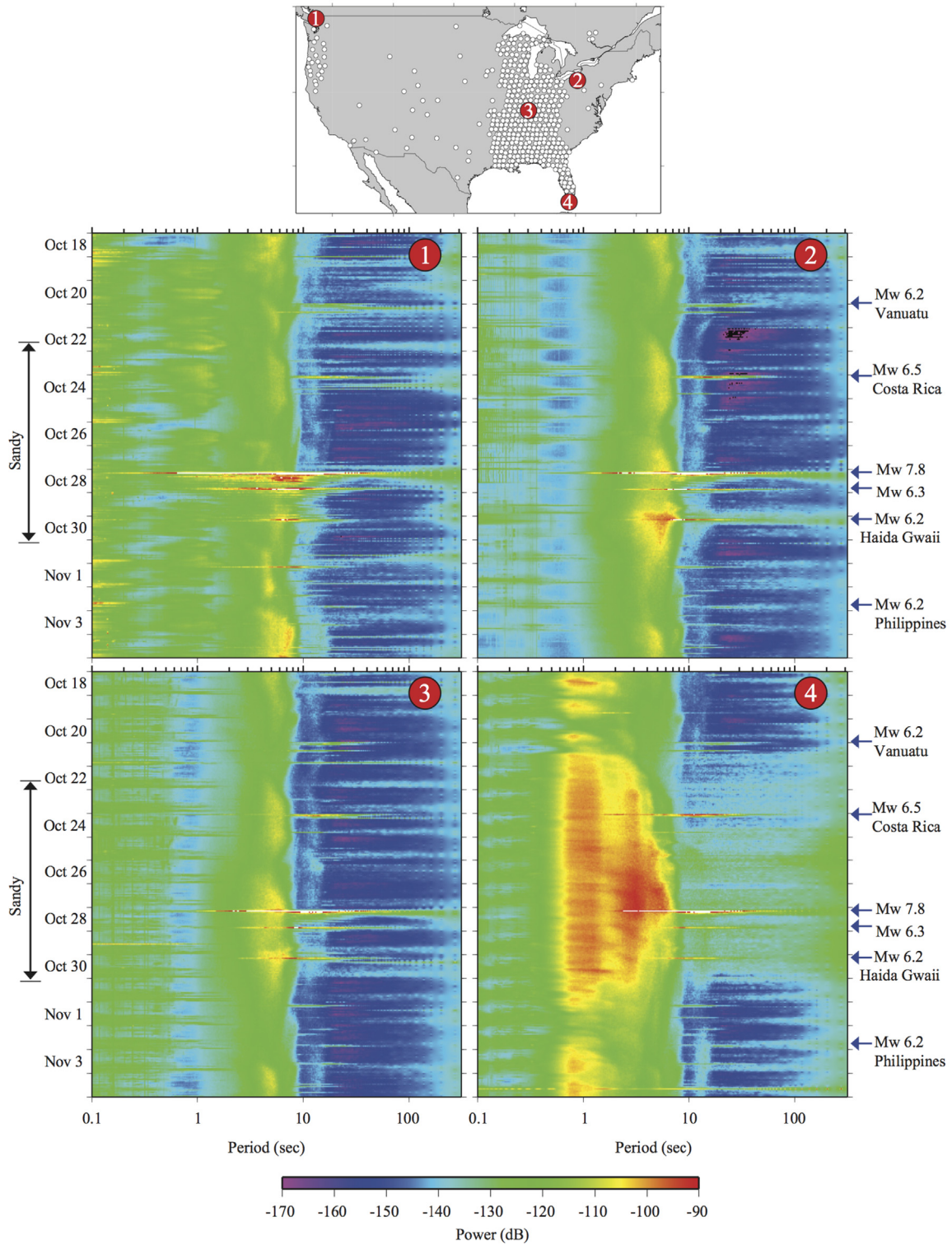


**Fig. 3.** Spectrograms of dominant eigenvalue power for four TA stations. Stations 1–4 correspond to TA stations A04D, M54A, S46A, and 062Z respectively. Earthquakes with magnitudes of at least  $6.0M_w$  are noted on the right with blue arrows, and time extent of Sandy is indicated on the left with the black arrows. (For interpretation of the references to color in this figure legend, the reader is referred to the web version of this article.)

$M_w$  7.8 Haida Gwaii event that occurred on October 28, 2012 and its aftershocks. Interestingly, the 5 s power is only slightly elevated during Sandy's passage compared to the normal background level. The 8 s power shows greater sensitivity to earthquake transients, however it also shows greater dynamic range than the 5 s curve in responding to microseisms. In at least one case, on November 3–4, the TA stations respond simultaneously to two different storm systems, with the double-frequency peak splitting into a dominant

sub-peak near 5 s and a weaker, narrower sub-peak near 8 s. The 12 s and 20 s bands show increasing sensitivity to earthquake transients with relatively subtle influence from single-frequency microseisms.

A strong diurnal pattern is evident over a broad range of periods. It is strongest at periods  $< 1.0$  s, which also show a weekly variation, implying that cultural factors such as traffic and construction are mainly responsible. Diurnal oscillation at longer

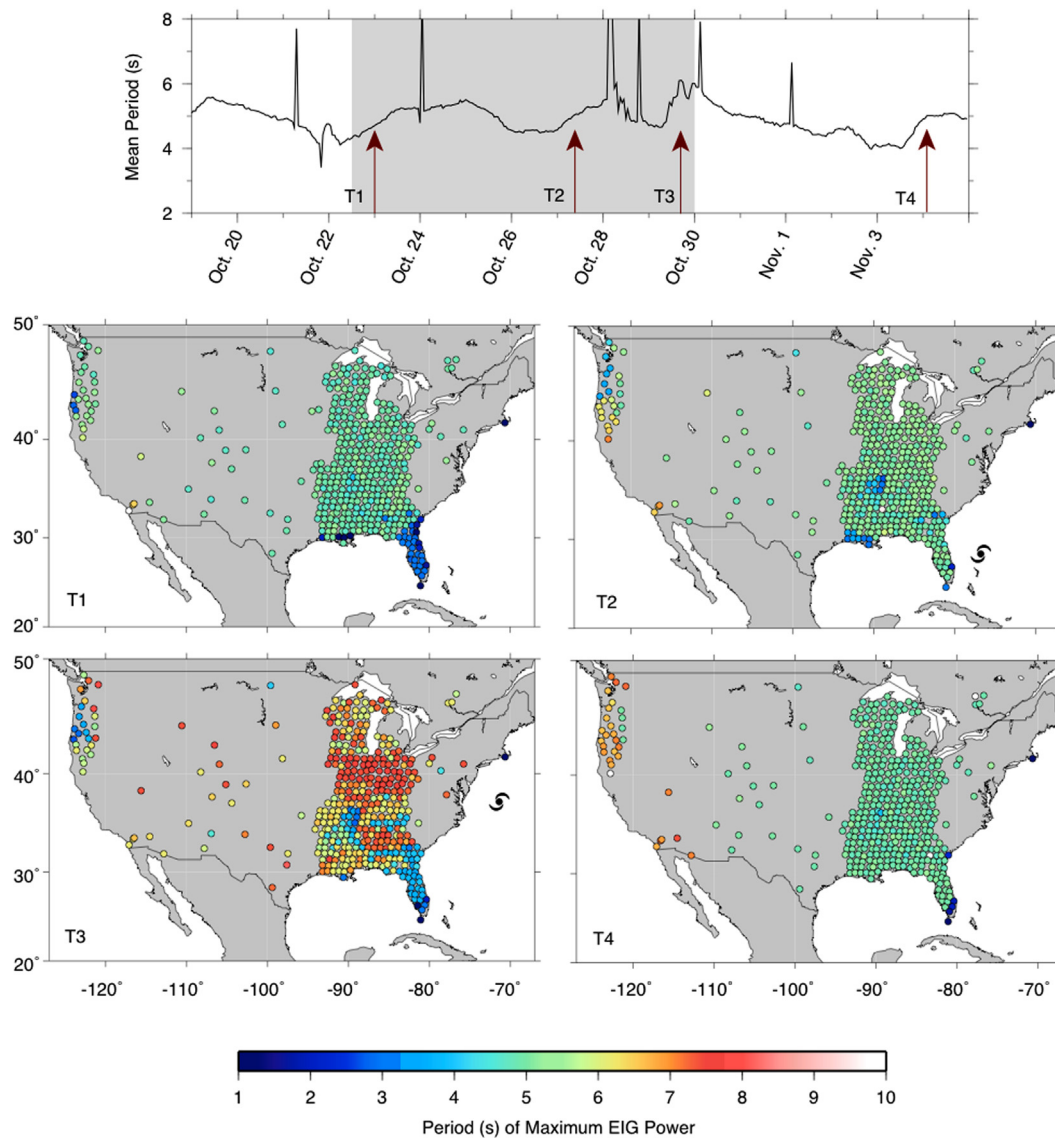


**Fig. 4.** Periods corresponding to the largest eigenvalue power in the microseismic band. The top panel shows the array-averaged period as a function of time, with grey shading used to indicate the time Sandy was active. The four bottom panels show the spatial variation in dominant period at the times indicated by arrows in the top panel.

periods,  $> 20$  s, lack a weekly signal and are more likely due to natural factors such as day–night temperature fluctuations that cause tilting of the seismometer which in turn gets recorded as horizontal accelerations.

### 3.2. Spectrograms of individual stations

Noise power at individual TA stations share the general time-frequency behavior shown in the array-averaged spectrogram (Fig. 2(a)), however there is significant variation related to site effects and local noise sources, and there is less of a diurnal signature compared to the array average. In Fig. 3 we show results from four representative stations: A04D located the northwest corner of the United States on Lummi Island, WA; M54A located southeast of Lake Erie in Oil City, PA; S46A located in the center of the TA in Corydon, KY; and station 062Z located on an island of the Florida Keys in Marathon, FL. We again use power measured from the largest eigenvalue of the spectral covariance matrix, ensuring that the dominant noise source is fully repre-

sented no matter how it is polarized or from which direction it arrives.

Unsurprisingly, the most prominent feature in the spectrogram of the TA station A04D in Washington is the signal from the  $M_w$  7.8 Haida Gwaii earthquake and its early aftershocks. The microseismic signal from Sandy is subtle and is less strong than the normal background microseisms that occurred before and after the passage of Sandy. This is probably due to the large distance of A04D from the east coast and the relatively high attenuation of seismic energy in the western U.S. The brightest microseism occurred November 3–4 with a dominant period near 8 s. A large peak occurs simultaneously at the corresponding single-frequency band, suggesting the microseismic energy was generated from a storm interacting with the coastline. The results using an ocean wave model (described later) and presented in Fig. 12, confirm the presence of the 8 s seismic noise sources along western Canada and Alaska. In general, the single-frequency peak tracks the larger double-frequency peak, showing the same sort of gliding dispersion as a function of time.

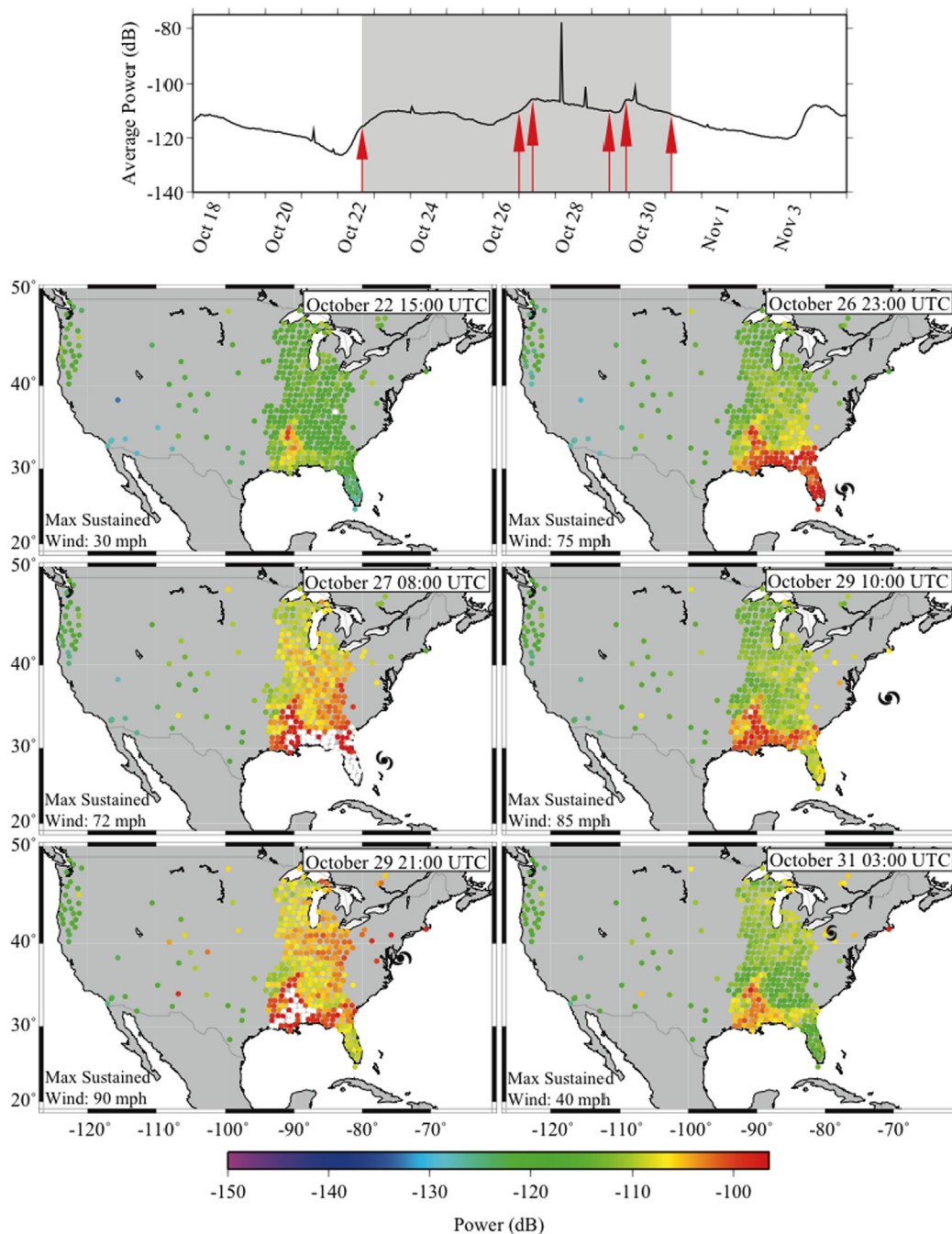


**Fig. 5.** Variation in 5 s power across space and time, where power is calculated from the dominant eigenvalue of the covariance matrix. The top panel shows the array-averaged variation in 5 s power with grey shading used during the time Sandy was active. The red arrows indicate times for which the spatial variation in 5 s power is shown below in an individual panel. A full animation is available in the electronic supplement. (For interpretation of the references to color in this figure legend, the reader is referred to the web version of this article.)

The TA station M54A, located near Lake Erie, shows a much stronger signal from Sandy. The peak near 5 s for October 29–31 is the largest on the spectrogram and coincides with a sharp change in direction of Sandy. At this time Sandy's path changed from the northeast to the northwest, and the speed along the path increased (Fig. 1). Other double-frequency microseism arrivals that are lower in power occurred around October 18, October 24, and November 3. The single frequency peak is visible almost throughout the entire period and often shows a dispersive gliding (e.g., October 21–22). As with other stations, this band was strongly contaminated by earthquake energy from the Haida Gwaii sequence. TA station S46A, located in Kentucky, shows features very similar

to M54A, but with a smaller peak from Sandy, presumably due to its greater distance from the storm.

One of the most distinctive spectrograms is from the TA station O62Z, located on an island in the Florida Keys. Strong power was observed at 1 s for the entire time that Sandy was active, even when it was south of Cuba with low wind speeds. Owing to the relatively short period, it's likely that this energy is related to an increase in local wind speeds. The strongest signal associated with Sandy occurs over a relatively wide band of 3–5 s, with peak energy associated with the Sandy turn over October 29–31. Interestingly, O62Z shows an increase in power at periods greater than 20 s, associated with the passage of Sandy. Significant power exists

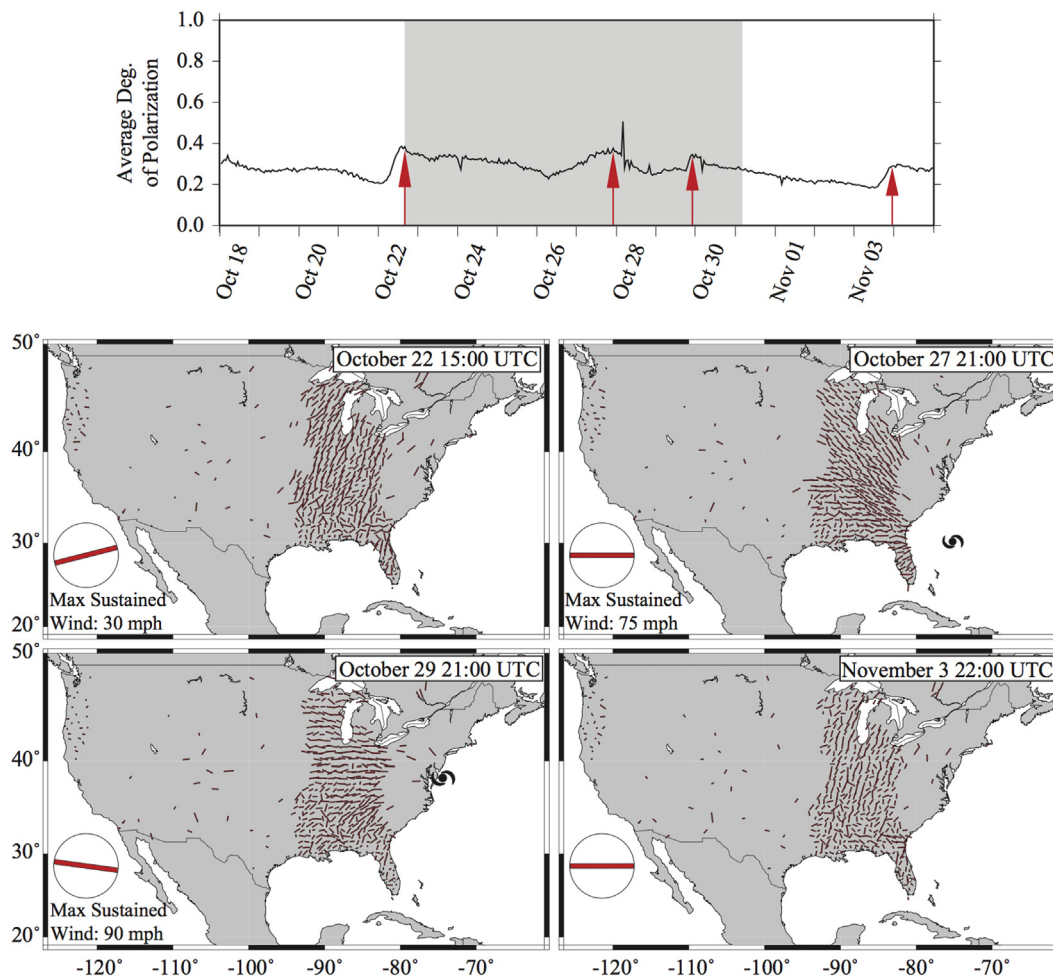


**Fig. 6.** Variations in the polarization of 5 s energy across space and time. The top panel shows the array-averaged variation in the degree of polarization,  $\beta^2$ . Grey shading is used to indicate the time extent of Sandy and the red arrows correspond to the times of the four panels shown below. Each panel shows the azimuthal orientation of the polarization ellipsoid,  $\Theta_H$ , at each station, with length scaled by  $\beta^2$ . The array-averaged value of  $\Theta_H$  is shown by the large red line in the lower left corner of each panel. Hurricane symbols are used to show the location of Sandy. A full animation is available in the electronic supplement. (For interpretation of the references to color in this figure legend, the reader is referred to the web version of this article.)

up to at least 300 s, and may be especially observable at 062Z because of its island, or coastal, setting.

### 3.3. Time evolution of the dominant microseismic period

As shown in the previous spectrogram figures, there is noticeable drifting of the dominant period (i.e., period with the highest power) within the microseismic band. In Fig. 4 we present the time and spatial evolution of these dominant periods, with a complete animation available in the electronic supplement. Site effects are clearly seen, with stations in Florida nearly always dominated by 1–3 s energy, while the remainder of the array is commonly characterized by 5–6 s energy. It is possible that unusual winds or the peninsular nature of Florida are partially responsible for the period reduction in microseismic noise; however, stations along the Gulf coast and further north along the Mississippi valley also often have reduced microseismic periods suggesting that the enhanced sediment thickness in these areas (e.g., Laske and Masters, 1997) preferentially traps shorter-period microseismic energy. It is only when Sandy passed north over the Bahamas Islands on October 27 that all the Florida stations have peak periods near 5 s.

The most dramatic feature seen in the animation of peak period is the sharp rise on October 29, at the time when Sandy makes an abrupt turn from the northeast to the northwest and increases the speed at which it is traveling. Here the dominant

periods across much of the TA quickly rise to 8–9 s and then gradually drop back to 5 s as Sandy approaches the coastline and makes landfall. The drift to long periods does not seem to be a path effect, in which shorter-period energy is preferentially attenuated, because the storm locus does not change significantly. Likewise, the wind speeds and bathymetry are similar before the turn and when the turn begins. Therefore, we attribute the increase in period to stronger wave–wave interaction as the storm turns.

### 3.4. Time evolution of the microseismic wavefield across the TA

We examined the distribution of power and polarization across the TA in spatial and time domains for a wide range of periods (0.5–200 s) but here we present results for the 5 s (Figs. 5, 6), 8 s (Figs. 7, 8), and 12 s (Figs. 9, 10) periods, focusing on the classic double-frequency and single-frequency microseism bands. The location of the hurricane's eye and the maximum sustained wind noted on the figures were taken from the Sandy Graphics Archive web page of the National Hurricane Center ([http://www.nhc.noaa.gov/archive/2012/graphics/al18/loop\\_3W.shtml](http://www.nhc.noaa.gov/archive/2012/graphics/al18/loop_3W.shtml)).

The first figure for each period (Figs. 5, 7, and 9) includes several frames that show spatial variation of dominant eigenvalue power across the TA, at the times indicated by arrows on the

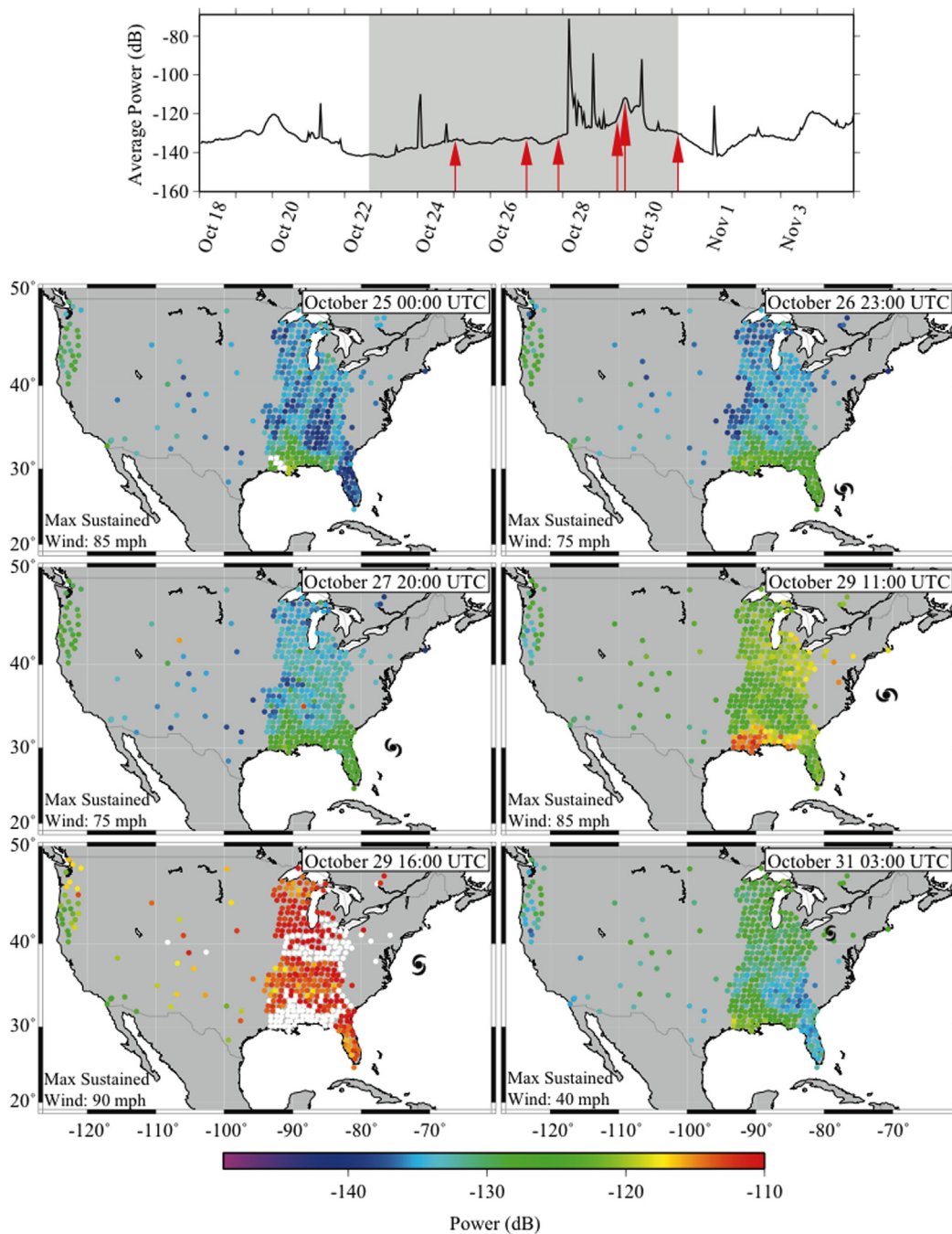


Fig. 7. The same as Fig. 5, but for a period of 8 s. A full animation is available in the electronic supplement.

array-averaged curve in the top panel. Earthquakes can be seen as spikes in the time series, whereas the microseismic arrivals can be seen as longer-period humps, with a gradual increase, possibly a flat top, and then a gradual decrease in power. Complete animations for each period are included in the electronic supplement.

The second figure associated with each period (Figs. 6, 8, and 10) includes several frames that show the spatial variation of  $\Theta_H$ , the horizontal azimuth of the major axis of the polarization ellipsoid, at specific times. The lengths of the vectors are weighted by the degree of polarization ( $\beta^2$ ), with more polarized ground motion having longer lines. The array-averaged value of  $\beta^2$  is shown as a function of time across the top panel, with red arrows indicating the time for each frame. As in the case of array-averaged power, earthquakes appear as spikes and microseismic arrivals ap-

pear as smooth humps. Complete animations for each period are included in the electronic supplement.

Unless otherwise noted, the observed energy is consistent with Rayleigh wave propagation. Histograms of phase differences between the vertical and dominant horizontal components ( $\varphi_{VH}$ ) are generally clustered around  $\pm 90^\circ$ . We note that the positive values do not necessarily indicate prograde motion, since they can also be interpreted as retrograde arrivals from the opposite direction,  $\Theta_H + / - 180^\circ$  (Park et al., 1987). In general, we find that selecting the direction corresponding to  $\varphi_{VH} \sim -90^\circ$  gives the expected result, however this is not universally true, especially when the degree of polarization is relatively low. This may be caused by numerical instability or perhaps actual prograde Rayleigh wave particle motion caused by an unusual velocity structure (Tanimoto

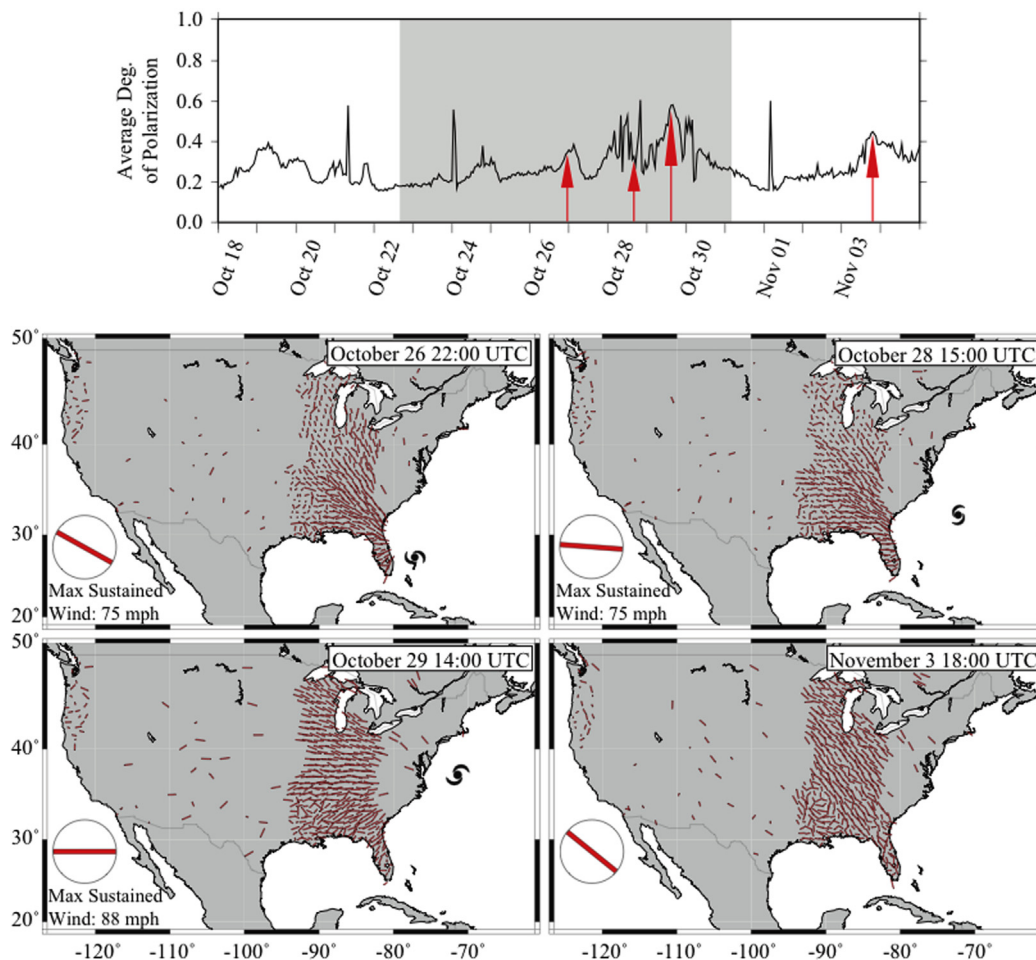


Fig. 8. The same as in Fig. 6, but for a period of 8 s. A full animation is available in the electronic supplement.

and Rivera, 2006). For this reason, we do not use heads on the vectors indicating  $\Theta_H$ .

#### 3.4.1. The 5 s microseismic wavefield

During the eighteen-day study period, the 5 s wavefield was the least contaminated by earthquakes in terms of power (Fig. 5) and degree of polarization (Fig. 6). The effects of Hurricane Sandy were observed beginning on October 25, as Sandy gained wind speed and began moving northward from Cuba as a category 1 hurricane. As Sandy reached the coast of Florida, the microseismic power increased and reached its first peak around October 27 08:00 UTC (the second and third time frames from Fig. 5). Following this first maximum, the microseismic energy decreased as Sandy moved away from the Florida coastline to the northeast. As Sandy approached the coasts of New Jersey, New York, and Delaware on October 29 21:00 UTC, the second maximum was observed in the array-averaged microseismic energy (the fifth time window in Fig. 5). After this point, Sandy lost its energy and rotation and became a post-tropical depression on land. This resulted in a significant decrease in the array-averaged energy (the sixth time frame in Fig. 5).

The power results are consistent with the degree of polarization figures (October 27, 21:00 UTC time frame and the October 29, 21:00 UTC time frame from Fig. 6). It can be seen that the station polarization vectors are pointing to one specific region for each time frame. The second time frame is associated with Hurricane Sandy's northeast motion, away from the Florida coastline and all the stations are pointing to the southeast of TA network. The third time frame is associated with the turning (westward motion, to-

wards Long Island, New York) and all the vectors are pointing to the west of TA network.

We also observed three domains in the array-averaged power not correlated with Sandy. The first domain in microseismic power was observed October 18–21 (Fig. 5). This decrease in power was most likely associated with the previous North Atlantic storm known as hurricane Rafael (National Hurricane Center, Hurricane Rafael advisory archive; [www.nhc.noaa.ov/archive/2012/RAFAEL.shtml](http://www.nhc.noaa.ov/archive/2012/RAFAEL.shtml)). Following this, there was a broad peak in the microseismic power on October 22–25 that coincided with the initiation of Sandy (October 22 15:00 UTC time frame, Fig. 5). The northeast-southwest polarized vectors from the first time frame in Fig. 6 indicate two possible source regions; northeast pointing to the North Atlantic or southwest direction pointing to the Gulf of Mexico. Assuming that the arrivals are standard retrograde Rayleigh waves, the  $\varphi_{VH}$  values near  $-90^\circ$  that are observed imply a North Atlantic origin. The third domain occurs November 3–4 (Fig. 5), with the polarization analysis again indicating a North Atlantic origin.

#### 3.4.2. The 8 s microseismic wavefield

The 8 s period is another interesting region in the double-frequency microseism band, with fluctuation in the array-averaged power curve greater than that observed for the 5 s period (Fig. 7). As Sandy approached the coast of Florida, there was an increase in power, and even as Sandy moved away from Florida to the northeast, this increasing trend continued until being interrupted by surface waves of  $M_w$  7.8 Haida Gwaii earthquake and its aftershocks. Following this interruption, the maximum amplitudes were

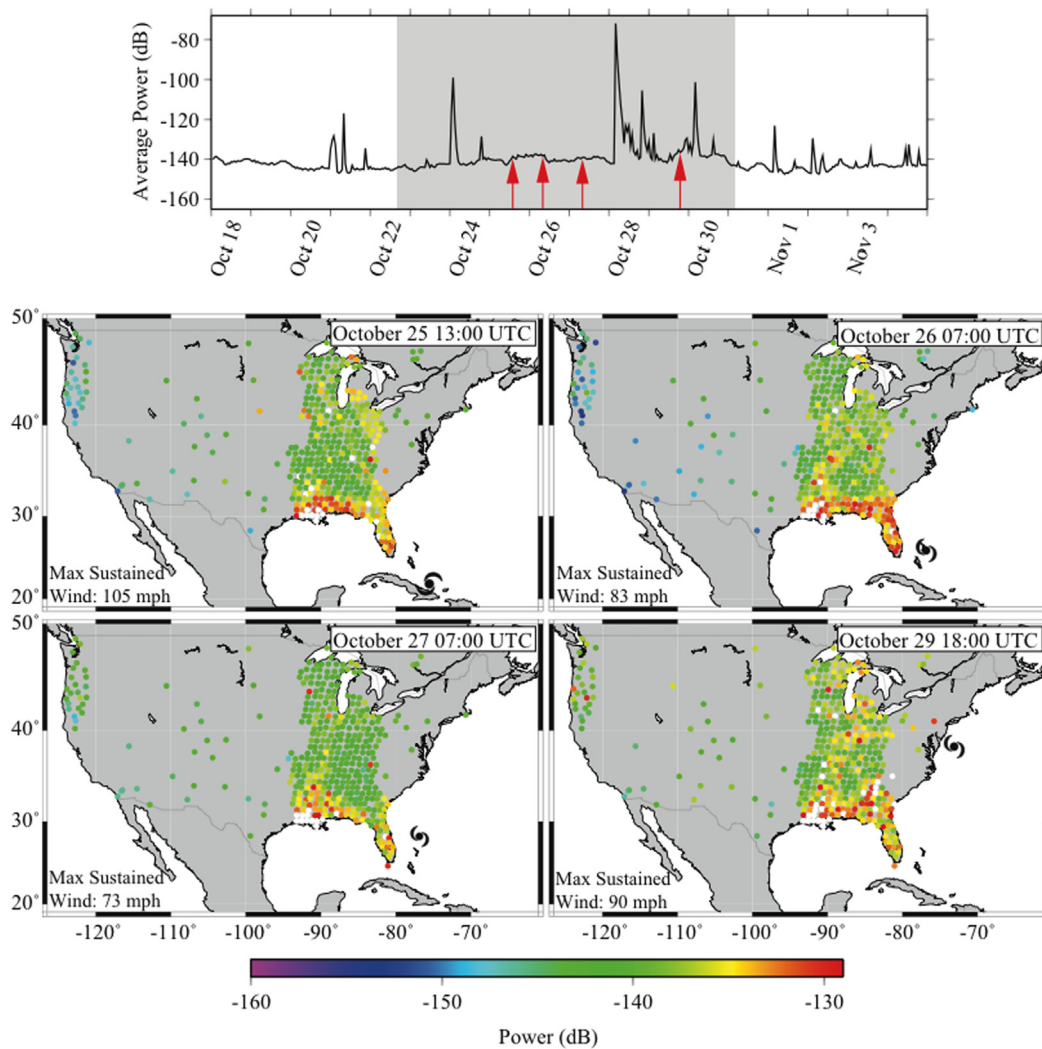


**Fig. 9.** The same as in Fig. 5, but for a period of 12 s. A full animation is available in the electronic supplement.

observed as Sandy made a turn to the west (towards New Jersey and Delaware) (October 29, 16:00 UTC time frame from Fig. 7). Following that, the microseismic energy started gradually decreasing as Sandy made landfall and became a post-tropical depression near Lake Erie (the last time frame from Fig. 7).

Our 8 s power results are complemented by the degree of polarization curve and the spatial polarization maps shown in Fig. 8. The first and third time frames indicate regions where the eight-second energy was generated. The first time frame (October 26, 22:00 UTC) points to the southeast when Sandy approached the coast of Florida. The third time frame (October 29, 14:00 UTC) points to the east of the TA when Sandy made its westward turn. These regions are probable microseismic source locations coinciding with Sandy's position. The second time frame in Fig. 8 (October 28, 15:00 UTC) is an exception in terms of coincidence of source region and Sandy's position. As seen from the map, the polarization vectors point to the south of Sandy's location. This shows the source region is located somewhere in the wake of the hurricane.

A final observation we make is the orientation of the polarization vectors for the map of November 3, 18:00 UTC. They are polarized in a northwest–southeast direction, different from the five-second energy that is polarized northeast–southwest during the same time period. Relative phase observations for the 8 s energy support retrograde Rayleigh waves arriving from somewhere in the Northern Pacific. These two different results indicate 5 s en-

ergy and 8 s energy are sensitive to source regions in different oceans.

An interesting feature of the 8 s power maps (Fig. 7) is finger-like striations that are aligned in the direction of the microseismic source. These features are apparent in the time frames of October 26 23:00 UTC, October 27 20:00 UTC, October 29 16:00 UTC from Fig. 7, but are most clearly viewed in the supplementary animation. These features were also seen during the passage of other distant storms and the Haida Gwaii earthquakes, and they always pointed towards the source. We think these patterns vary too quickly with azimuth to be related to any irregular near-source bathymetric feature, and instead are related to the focusing and defocussing of energy propagating in a 3D Earth.

### 3.4.3. The 12 s microseismic wavefield

The single frequency microseism band is generally defined between 10 s and 16 s. Although each period in this band is sensitive to different aspects of microseisms, we present the 12 s energy because of its strong response to Sandy's motion towards Florida. With the exception of earthquakes, the 12 s microseismic power did not vary nearly as much as it did for 5 s and 8 s periods. However, the second time frame (October 26 07:00 UTC) and particularly the fourth time frame (October 29 18:00 UTC) in Fig. 9 indicate a rise in power across the TA stations. Increased amplitudes are seen when Sandy reached the shallow waters of Florida and when Sandy changed course to the west. However, the westward

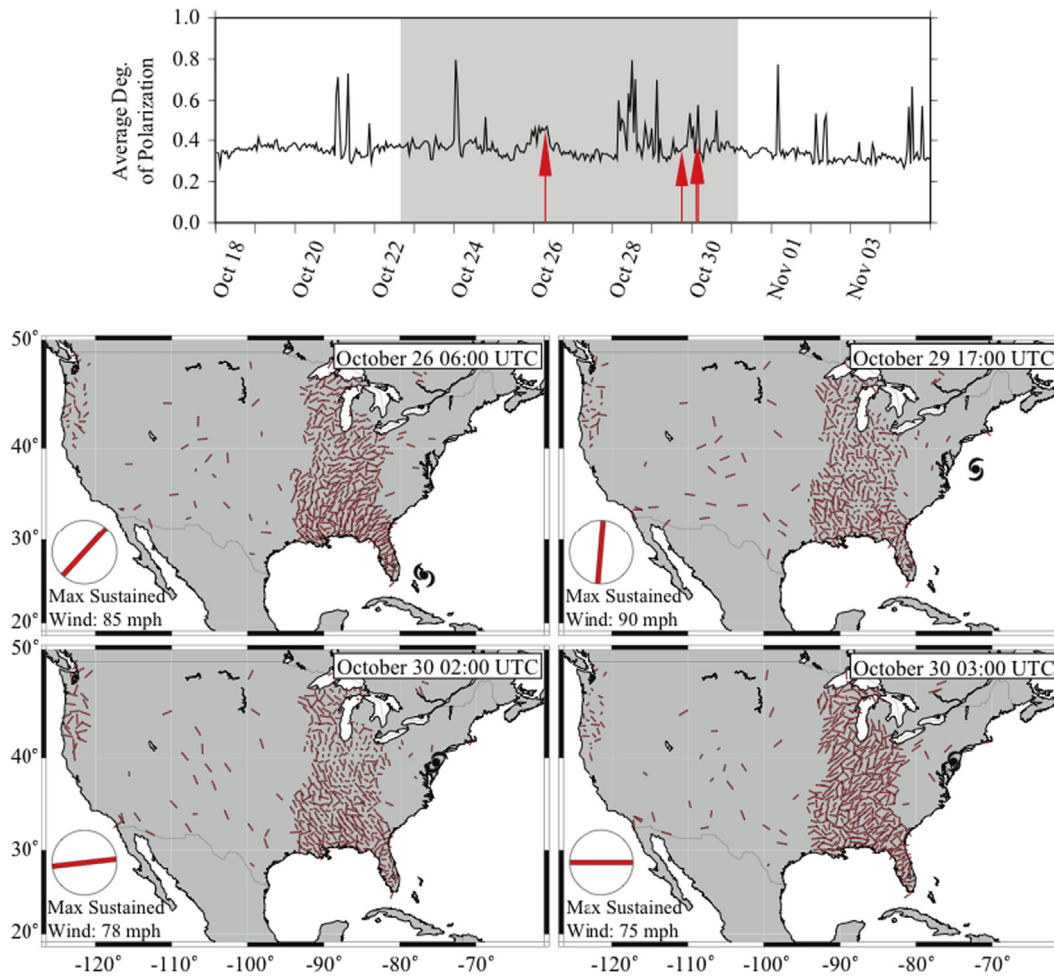


**Fig. 10.** The same as in Fig. 6, but for a period of 12 s. A full animation is available in the electronic supplement.

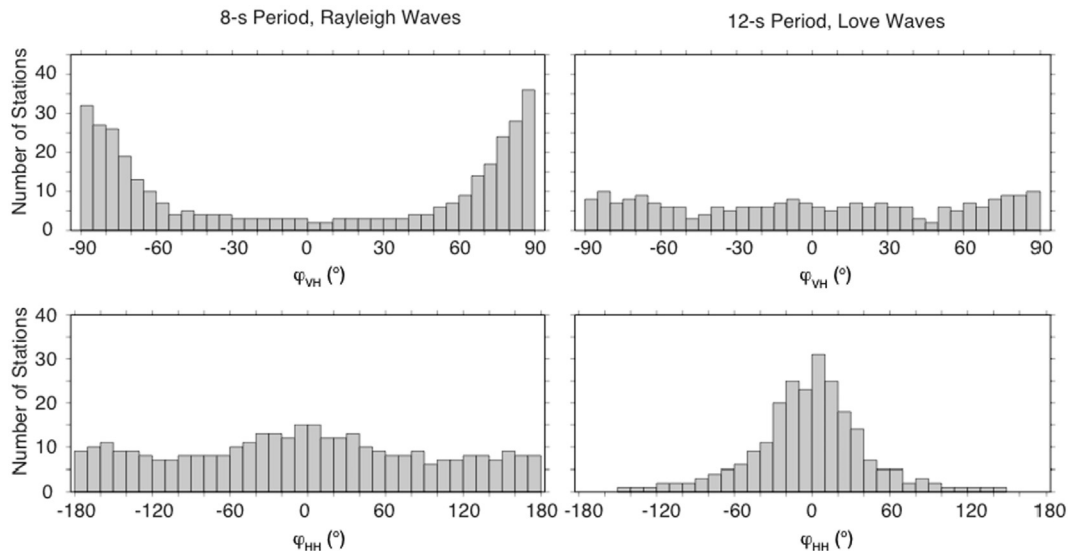


**Fig. 11.** Distribution of phase differences between the vertical and dominant horizontal components ( $\varphi_{VH}$ ) and the two horizontal components ( $\varphi_{HH}$ ). The panels on the left are typical of energy recorded at 5 s and 8 s throughout the study period, while the panels on the right correspond to stations showing azimuthal polarization orientation ( $\varphi_{HH}$ ) at 12 s that is orthogonal to the direction of Sandy. In both cases, eigenvectors were analyzed for a 16 hr period (October 25, 19:00 UTC through October 26 10:00 UTC) for those stations with  $\beta^2 > 0.15$ .

turn is mostly masked by the  $M_w$  7.8 Haida Gwaii mainshock and its aftershocks.

Weak, but recognizable, finger-like radiation patterns are also observed in this period and other nearby periods of the single

frequency microseism band (October 26 07:00 UTC time frame in Fig. 9). The higher degree-of-polarization values coincide with the time period when these patterns are present (Fig. 10). The most interesting observation in the 12 s band is the azimuthal orientation

of the polarization vectors. The first time frame in Fig. 10 shows polarization vectors oriented orthogonal to those from the 5 s and 8 s periods, suggesting Love wave particle motion. This idea is reinforced by considering the phase differences between the horizontal and vertical components. In Fig. 11, we compare histograms of  $\varphi_{HH}$  and  $\varphi_{VH}$  for the prospective 12 s Love waves to those from typical 8 s Rayleigh waves. For the prospective Love waves the  $\varphi_{HH}$  distribution is strongly peaked around  $0^\circ$ , while the  $\varphi_{VH}$  distribution is flat across all angles, indicative of linearly polarized motion in the horizontal plane with insignificant motion on the vertical component. The Rayleigh waves, in contrast, have a flat  $\varphi_{HH}$  distribution and a  $\varphi_{VH}$  distribution strongly peaked around  $\pm 90^\circ$ , indicative of elliptical particle motion in the vertical-radial plane and insignificant motion on more than one horizontal component.

It is unclear precisely how Love waves are generated from ocean waves, and here we speculate that they may be generated by the interaction of storm/hurricane-induced ocean waves with small-wavelength bathymetric features (such as small islands and seamounts) that act as secondary, Huygens-type sources of seismic energy. In order to validate this hypothesis, synthetic modeling of the 3D coupled ocean–solid Earth system is required.

#### 4. Discussion and conclusions

Analysis of microseisms created by Superstorm Sandy and recorded across the TA shows that the overall strength of the microseismic energy varied considerably as the storm progressed. As expected, double-frequency microseismic energy was dominant, with the peak energy occurring on October 29 as the storm shifted sharply to the northwest and accelerated. A smaller peak occurred on October 27 as the storm crossed over the Bahamas and turned toward the northeast. In both of these cases, and more generally throughout the observation period, the dominant period was positively correlated with power, varying mainly between 5 s and 8 s. The TA-averaged microseismic power created by Sandy was only slightly

larger than the background microseismic power created by storms in the North Atlantic and North Pacific at around the same time. For instance, North Atlantic storms occurring around October 22–23 and November 3–4 generated microseisms with a dominant period near 5 s and nearly the same power as Sandy. Likewise, a northeastern Pacific storm on November 3–4 generated significant microseismic power at a period near 8 s.

The polarization vectors of the 5 s and 8 s energy tracked the motion of Hurricane Sandy closely. They generally pointed towards the eye of the hurricane as the source region, but also sometimes lagged slightly behind the eye, pointing to a source region in the storm's wake. The TA-averaged degree of polarization was positively correlated with average power and period, and peaked when Sandy sharply turned direction on October 27 and October 29. In general, the polarization analysis indicated that Sandy created mainly Rayleigh wave energy, with evidence of Love wave generation in the single-frequency band as the storm passed over the Bahamas.

Fig. 12 shows the computed daily averages of the power spectral density of the equivalent pressure generated by the ocean surface gravity waves (Arduin and Herbers, 2013) using the Ifremer version 4.07 of the WAVEWATCH-III ocean wave model (Tolman, 2002). The global model has a spatial resolution of  $0.5^\circ$  in latitude and longitude and incorporates coastal reflections. (A discussion of the model parameterization is presented in Arduin et al., 2011.) The frames for the dates of October 27 and October 29 show significant wave–wave interactions (for seismic periods of 5 s and 8 s) occurring close to the Florida coastline, and off the coasts of New Jersey, Delaware and New York, respectively. Our results of 5 s and 8 s polarization vectors were pointing towards these regions where

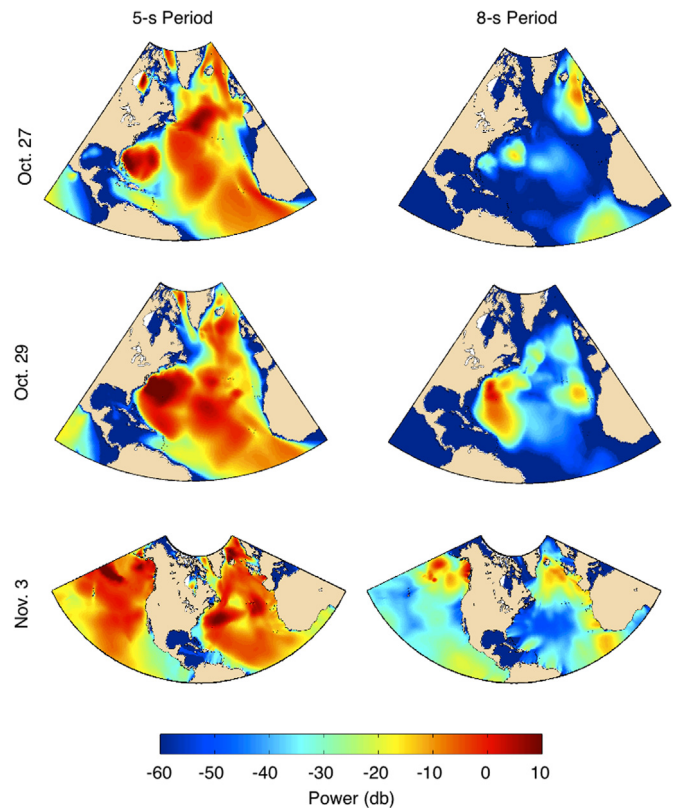


Fig. 12. Daily averaged power spectral density of the equivalent pressure generated by the ocean surface gravity waves, corresponding to seismic periods of 5 s and 8 s, computed from the WAVEWATCH-III Ifremer model. The units (db) correspond to  $10 \log_{10}(\text{m}^4/\text{Hz})$ . The top frames show the time when Sandy approached the Florida coastline (October 27) and the middle frames show the power spectral density at the time when Sandy made the sharp westward turn (October 29). The bottom frames indicate the modeled power for the North Atlantic and Pacific oceans for the time when the splitting of the double frequency microseism band occurred (November 3).

the maximum in spectral power was predicted by the ocean wave model for those specific dates. We also observed a similar situation for microseisms not related to Sandy. On November 3, there were two different regions with peak spectral power, one in the North Atlantic located off the east coast of Greenland (5 s) and another region in the Northeast Pacific (8 s). These regions are also consistent with the polarization vectors of 5 s and 8 s periods from the November 3, 22:00 UTC time frame in Fig. 6, and the November 3, 18:00 UTC time frame in Fig. 8. This explains the splitting of double frequency microseism band for the dates of November 3–4 in the array-averaged spectrogram (Fig. 2).

Arduin et al. (2011) recently presented a classification system for microseismic generation from wave–wave interactions in the ocean. They based their classification on sea states with the following definitions: class-I is the mechanism where ocean waves generated by a rapidly moving storm interact with trailing waves in the opposite direction; class-II involves coastally reflected ocean waves interacting with the incident waves propagating in the opposite direction; and the class-III mechanism is the interaction of ocean wave groups generated by two separate storm systems. Considering the directions of 5 s and 8 s polarization vectors for October 27 and October 29, and the results from the numerical ocean wave model, we conclude that the microseisms from Sandy were generated mainly by a class-I mechanism type (similar to the mechanism IIIa described in Fig. 2a by Arduin et al., 2011).

## Acknowledgements

The figures were made using GMT v4.2.0 (Wessel and Smith, 1991) and the data were obtained from the IRIS DMC. This work was funded by NSF-Earthscope under award EAR-0951558. We thank the Marine Modeling Center at the National Centers for making WAVEWATCH-III data available and thank Arun Chawla for assistance with those data during a preliminary portion of this study. We thank Fabrice Arduin for making his Matlab code and the microseismic source models available. Comments from two anonymous reviewers were very helpful.

## Appendix A. Supplementary material

Supplementary material related to this article can be found online at <http://dx.doi.org/10.1016/j.epsl.2013.10.015>.

## References

- Arduin, F., Stutzmann, E., Schimmel, M., Mangeny, A., 2011. Ocean wave sources of seismic noise. *J. Geophys. Res.* 116 (C09004). <http://dx.doi.org/10.1029/2011JC006952>.
- Arduin, F., Herbers, T.H.C., 2013. Noise generation in the solid earth, oceans, and atmosphere, from nonlinear interacting surface gravity waves in finite depth. *J. Fluid Mech.* 716, 316–348. <http://dx.doi.org/10.1017/jfm.2012-548>.
- Aster, R.C., McNamara, D.E., Bromirski, P.D., 2008. Multidecadal climate-induced variability in microseisms. *Seismol. Res. Lett.* 79 (2), 194–202.
- Aster, R.C., McNamara, D.E., Bromirski, P.D., 2010. Global trends in extremal microseism intensity. *Geophys. Res. Lett.* 37 (L14303). <http://dx.doi.org/10.1029/2010GL043472>.
- Behr, Y., Townend, J., Bowen, M., Carter, L., Gorman, R., Brooks, L., Bannister, S., 2013. Source directionality of ambient seismic noise inferred from three-component beamforming. *J. Geophys. Res.* 118, 240–248. <http://dx.doi.org/10.1029/2012JB009382>.
- Chevrot, S., Sylvander, M., Benahmed, S., Ponsolles, C., Lefèvre, J.M., Paradis, D., 2007. Source locations of secondary microseisms in western Europe: Evidence for both coastal and pelagic sources. *J. Geophys. Res.* 112 (B11301). <http://dx.doi.org/10.1029/2007JB005059>.
- Chi, W.-C., Chen, W.-J., Kuo, B.-Y., Dolenc, D., 2010. Seismic monitoring of western Pacific typhoons. *Mar. Geophys. Res.* 31, 239–251. <http://dx.doi.org/10.1007/s11001-010-9105-x>.
- Earle, P.S., 1999. Polarization of the Earth's teleseismic wavefield. *Geophys. J. Int.* 139, 1–8.
- Ebeling, C.W., Stein, S., 2011. Seismological identification and characterization of a large hurricane. *Bull. Seismol. Soc. Am.* 101 (1), 399–403. <http://dx.doi.org/10.1785/0120100175>.
- Gerstoft, P., Fehler, M.C., Sabra, K.G., 2006. When Katrina hit California. *Geophys. Res. Lett.* 33 (L17308). <http://dx.doi.org/10.1029/2006GL027270>.
- Grevemeyer, I., Herber, R., Essen, H.-H., 2000. Microseismological evidence for a changing wave climate in the northeast Atlantic Ocean. *Nature* 408, 349–352.
- Harris, D., 1990. Comparison of the direction estimation performance of high-frequency seismic arrays and three-component stations. *Bull. Seismol. Soc. Am.* 80, 1951–1968.
- Hasselmann, K., 1963. A statistical analysis of the generation of microseisms. *Rev. Geophys.* 1, 177–209.
- Jurkevics, A., 1988. Polarization analysis of three-component array data. *Bull. Seismol. Soc. Am.* 78, 1725–1743.
- Kedar, S., Longuet-Higgins, M., Graham, F.W.N., Clayton, R., Jones, C., 2008. The origin of deep ocean microseisms in the North Atlantic Ocean. *Proc. R. Soc. Lond. Ser. A, Math. Phys. Sci.* 464, 1–35. <http://dx.doi.org/10.1098/rspa.2007.0277>.
- Koper, K.D., de Foy, B., Benz, H., 2009. Composition and variation of noise recorded at the Yellowstone Seismic Array, 1991–2007. *J. Geophys. Res.* 114 (B10310). <http://dx.doi.org/10.1029/2009JB006307>.
- Koper, K.D., Hawley, V.L., 2010. Frequency dependent polarization analysis of ambient seismic noise recorded at a broadband seismometer in the Central United States. *Earthquake Sci.* 23, 439–447.
- Landès, M., Hubans, F., Shapiro, N.M., Paul, A., Campillo, M., 2010. Origin of deep ocean microseisms by using teleseismic body waves. *J. Geophys. Res.* 115 (B05302). <http://dx.doi.org/10.1029/2009JB006918>.
- Landsea, C., 2007. Counting Atlantic tropical hurricanes back to 1900. *Eos Trans. AGU* 88, 197–208.
- Laske, G., Masters, G., 1997. A global digital map of sediment thickness. *EOS Trans. AGU* 78, F483.
- Lay, T. (Ed.), 2009. *Seismological Grand Challenges in Understanding Earth's Dynamic Systems*. Report to the National Science Foundation, IRIS Consortium, 76 pp.
- Longuet-Higgins, M.S., 1950. A theory for the generation of microseisms. *Philos. Trans. R. Soc. Lond. Ser. A, Math. Phys. Sci.* 243, 1–35.
- Obrebski, M., Arduin, F., Stutzmann, E., Schimmel, M., 2013. Detection of microseismic compressional (P) body waves aided by numerical modeling of oceanic noise sources. *J. Geophys. Res.* 118. <http://dx.doi.org/10.1002/jgrb.50233>.
- Park, J., Vernon, F.L., Lindberg, C.R., 1987. Frequency dependent polarization analysis of high-frequency seismograms. *J. Geophys. Res.* 92, 12664–12674.
- Peterson, J., 1993. Observations and modeling of seismic background noise. USGS Open File Report 93-322. 94 pp.
- Rhie, J., Romanowicz, B., 2004. Excitation of Earth's continuous oscillations by atmosphere–ocean–seafloor coupling. *Nature* 431, 552–556.
- Samson, J.C., 1983. Pure states, polarized waves, and principal components in the spectra of multiple, geophysical time-series. *Geophys. J. R. Astron. Soc.* 72, 647–664.
- Schimmel, M., Stutzmann, E., Arduin, F., Gallart, J., 2011. Polarized Earth's ambient microseismic noise. *Geochem. Geophys. Geosyst.* 12, Q07014. <http://dx.doi.org/10.1029/2011GC003661>.
- Schulte-Pelkum, V., Earle, P.S., Vernon, F.L., 2004. Strong directivity of ocean-generated seismic noise. *Geochem. Geophys. Geosyst.* 5 (Q03004). <http://dx.doi.org/10.1029/2003GC000520>.
- Stutzmann, E., Schimmel, M., Patau, G., Maggi, A., 2009. Global climate imprint on seismic noise. *Geochem. Geophys. Geosyst.* 10 (Q11004). <http://dx.doi.org/10.1029/2009GC002619>.
- Suteau-Henson, A., 1990. Estimating azimuth and slowness from three-component and array stations. *Bull. Seismol. Soc. Am.* 80, 1987–1998.
- Tanimoto, T., Ishimaru, S., Alvizuri, C., 2006. Seasonality in particle motion in microseisms. *Geophys. J. Int.* 166, 253–266.
- Tanimoto, T., Rivera, L., 2006. Prograde Rayleigh wave particle motion. *Geophys. J. Int.* 162, 399–405.
- Tolman, H.L., 2002. User manual and system documentation of WAVEWATCH-III version 2.22. NOAA/NWS/NCEP/OMB Technical Note 222. 133 p.
- Traer, J., Gerstoft, P., Bromirski, P.D., Shearer, P.M., 2012. Microseisms and hum from ocean surface gravity waves. *J. Geophys. Res.* 117 (B11307). <http://dx.doi.org/10.1029/2012JB009550>.
- Wessel, P., Smith, W.H.F., 1991. Free software helps map and display data. *EOS Trans. AGU* 72, 445–446.